Observation of the pressure effect in simulations of droplets splashing on a dry surface

A. M. P. Boelens,[1] A. Latka,[2] and J. J. de Pablo[3,*]
[1]*Department of Energy Resources Engineering, Stanford University, 397 Panama Mall, Stanford, California 94305, USA*
[2]*Department of Physics, University of Chicago, 5720 South Ellis Avenue, Chicago, Illinois 60637, USA*
[3]*Institute for Molecular Engineering, University of Chicago, 5801 South Ellis Avenue, Chicago, Illinois 60637, USA*

(Received 4 February 2017; published 7 June 2018)

At atmospheric pressure, a drop of ethanol impacting on a solid surface produces a splash. Reducing the ambient pressure below its atmospheric value suppresses this splash. The origin of this so-called pressure effect is not well understood, and this study presents an in-depth comparison between various theoretical models that aim to predict splashing and simulations. In this paper, the pressure effect is explored numerically by resolving the Navier-Stokes equations at a 3-nm resolution. In addition to reproducing numerous experimental observations, it is found that different models all provide elements of what is observed in the simulations. The skating droplet model correctly predicts the existence and scaling of a gas film under the droplet, the lamella formation theory is able to correctly predict the scaling of the lamella ejection velocity as a function of the impact velocity for liquids with different viscosity, and lastly, the dewetting theory's hypothesis of a lift force acting on the liquid sheet after ejection is consistent with our results.

DOI: 10.1103/PhysRevFluids.3.063602

I. INTRODUCTION

A wide variety of outcomes can occur when a liquid droplet hits a dry solid surface. Depending on the impact velocity, surface tension, viscosity, ambient pressure, and surface roughness, one can observe deposition, splashing, receding breakup, or a rebound of the droplet [1]. The effect of ambient pressure on the transition between the smooth droplet-deposition and the splashing regimes is particularly intriguing. While intuition suggests that pressure should have a stabilizing effect, it has been found that lowering, instead of increasing, the ambient pressure suppresses splashing [2]. Despite various attempts to capture this so-called "pressure effect" in numerical simulations [3–5], its origins are still unknown. This knowledge gap has hindered technological developments, as there are numerous applications that could benefit from control over the splashing of droplets, including erosion, coating, cleaning, cooling, high-throughput drug screening, and fabrication techniques that rely on inkjet printing technology [6,7].

When surveying the literature on splashing experiments, two different observations of the effect of the ambient gas pressure on splashing have been reported: (i) The effect of pressure that can most readily be observed is that, assuming the crown of the splash at atmospheric pressure reaches a certain height, as pressure gets reduced, the height of the splash decreases [2], and (ii) when observing the splash using ultrafast interference imaging [8], a thin gas film can be observed under the liquid

*depablo@uchicago.edu

sheet that was ejected from the droplet upon impact. As the ambient pressure is reduced, at a certain threshold pressure, this gas film is no longer observed [9].

These two observations also help to illustrate the challenges associated with the multiscale nature of splashing. Length scales range from the contact line, where intermolecular forces act at nanometer length scales, to the characteristic length scale of the droplet itself, typically on the order of millimeters or larger. Timescales range from microseconds before impact, when deformation of the droplet leads to formation of the "central" air bubble [8,10,11], to milliseconds after impact when, as the liquid spreads radially in a thin film or lamella, the liquid sheet that was ejected from this lamella breaks up into many smaller droplets. While past efforts have tried to identify a single splashing criterion [12,13], all these length and timescales must be resolved or modeled in order to fully capture the physics of splashing.

In this paper, by fully resolving the Navier-Stokes equations, we reproduce the pressure effect on splashing and, in doing so, reveal a number of features that help explain its origins. This is achieved by performing calculations with spatial and temporal resolutions as high as 3 nm and 0.5 ps. These are length and timescales which are currently inaccessible to experiments. To obtain such high resolution, the simulations of droplets splashing on a dry surface presented in this paper are restricted to a two-dimensional axisymmetric geometry.

In addition to reproducing the pressure effect, the simulations describe several experimentally observed phenomena, including the formation of the central air bubble [8,10], the formation and ejection of a liquid sheet [8,14], and the contact-line instability leading to entrainment of gas bubbles at the liquid/gas interface [15]. A parameter sweep of lamella formation, varying impact velocity, viscosity, and surface tension allows us to evaluate three recently proposed theories of splashing and lamella formation. One of these proposes air entrainment at the contact line, also known as dewetting [16], as well as the existence of a lift force [17] as the mechanisms responsible for liquid-sheet formation and breakup. Another theory attributes splashing to a "skating" motion of the droplet on a thin gas film, and the deflection of liquid on the impact surface [11]. The third theory [18] proposes that lamella formation is caused by the interaction of viscous and inertial length scales.

The simulations show that upon impact a very thin gas film is present under the droplet. While at high enough impact velocities this gas film is not stable and tends to collapse, it is always present at the edge of the spreading droplet. This is because the contact line moves at high speed along the surface in a "rolling" fashion, continuously extending the gas film at the edge of the droplet. The observed scaling of the height of this very thin gas film as a function of the impact velocity is consistent with literature [11,19]. Simulation results for an increased slip length on the wall for the gas phase are consistent with the hypothesis that the breakdown of the continuum assumption introduces a slip length on the wall which is pressure dependent [20]. This provides a possible explanation for the experimental observation of a threshold pressure for splashing as mentioned above [9].

While it is not possible to identify the correct scaling of the lamella ejection velocity as a function of the impact velocity from the currently available simulation data, the lamella formation theory is the only model that captures the effect of viscosity as found in the simulations. In addition, evidence is found for the existence of an early-time viscous length scale for the height of the lamella as proposed in the lamella formation theory [18], and a different surface-tension-based length scale is found. Pertaining to the breakup of the liquid sheet, our results support the concept of a lift force acting on the liquid sheet, which was proposed as part of the dewetting theory. Our results disagree with the idea suggested by the skating droplet theory that it is the deflection of liquid on the solid surface that causes a drop to splash.

II. THEORY AND METHOD

To facilitate the tracking of topological changes, a volume of fluid (VOF) approach [21] is adopted in this paper. The VOF approach evolves around the definition of a phase parameter α with the

following properties,

$$\alpha = \begin{cases} 0 & \text{in gas phase,} \\ (0,1) & \text{on interface,} \\ 1 & \text{in liquid phase.} \end{cases} \tag{1}$$

The evolution of α is calculated using the following transport equation,

$$\frac{\partial \alpha}{\partial t} + \nabla \cdot (\alpha \vec{v}) + \nabla \cdot (\alpha(1-\alpha)\vec{v}_{lg}) = 0, \tag{2}$$

where $\vec{v}$ is the phase averaged velocity, and $\vec{v}_{lg}$ is a velocity field suitable to compress the interface. This equation is equivalent to a material derivative, but rewritten to minimize numerical diffusion [22].

The phase parameter is used to calculate the phase averaged density ρ, velocity $\vec{v}$, and viscosity μ, which are used in the momentum balance,

$$\frac{\partial \rho \vec{v}}{\partial t} + \nabla \cdot (\rho \vec{v} \otimes \vec{v}) = -\nabla p + \nabla \cdot (\mu \nabla \vec{v}) + \rho \vec{g} - \vec{f}, \tag{3}$$

and the continuity equation,

$$\nabla \cdot \vec{v} = 0. \tag{4}$$

In the above equations t is time, p is pressure, g is gravity, $\vec{f}$ is any body force, such as the surface-tension force, and $\otimes$ is the dyadic product. To complete the VOF model, an expression is needed to calculate the surface-tension force $\vec{f}_{\text{st}}$, and the initial and boundary conditions need to be chosen. The surface-tension force is calculated using the expression [23]

$$\vec{f}_{\text{st}} = \sigma_{\text{st}} \kappa \nabla \alpha, \tag{5}$$

where σ_{st} is the surface-tension coefficient, and κ is the curvature of the interface.

The computational domain has two different kinds of boundary conditions for each variable; on the bottom there is the impact wall, and on the sides and top there are boundary conditions which allow for the in- and outflow of gas. As a boundary condition for α on the impact wall, the generalized Navier boundary condition (GNBC) is used [24,25]. With this boundary condition the dynamic contact angle is allowed to vary freely, but a restoring line-tension force is applied at the contact line whenever the dynamic angle deviates from the equilibrium contact angle. This restoring force is an additional source term in the Navier-Stokes equations, and has the following form,

$$\vec{f}_{\text{lt}} = -\frac{\sigma_{\text{st}}}{h} \cos\theta_0 \nabla_{\text{2D}} \alpha. \tag{6}$$

This force is applied on the liquid-gas interface in the first grid cells next to the wall and balances the surface-tension force when the dynamic contact angle θ is equal to θ_0. In the above equation, σ_{st} is the surface-tension coefficient, $h = V/A$ is the mesh height, with A the surface area of the wall in a grid cell, and V its volume, and $\nabla_{\text{2D}}\alpha$ is the gradient of α on the wall. More information on the derivation and validation of this boundary condition can be found in Ref. [26]. On the wall the velocity obeys the Navier-slip boundary condition with a slip length of $\lambda_{\text{N}} = 1$ nm. While the slip length for the gas phase should be larger than this value, a value of 1 nm is realistic for a contact line. For mass conservation, the boundary condition for the pressure enforces both a zero flux and a zero second derivative of the pressure normal to the wall.

On the other sides of the simulation box, the phase parameter α obeys a Dirichlet fixed-value boundary condition for inflow and a zero-gradient Neumann boundary condition for outflow. The Dirichlet fixed value is set to zero, which is equivalent to only allowing gas to flow in. For each grid cell next to a sidewall the local inflow velocity is calculated from the wall-face normal component of the velocity vector associated with the center of that specific grid cell. The boundary condition

for the outflow velocity is a zero-gradient Neumann boundary condition. The total pressure p_0 on the sidewalls is kept constant according to a simplified Bernoulli's equation,

$$p_0 = p + \tfrac{1}{2}\rho|\vec{v}|^2. \tag{7}$$

In this boundary condition the gas is assumed inviscid, and when the gas inflow velocity $\vec{v}$ changes, the pressure p changes accordingly. The above equations are solved using the VOF solver of the OPENFOAM finite volume toolbox [27].

The accurate description of the velocity and pressure fields upon impact requires that the deformation of the droplet be captured as it falls. To allow the droplet to equilibrate with the gas flow around it, the droplet first falls through a large simulation box of 1×5 mm at a relatively low resolution of 320×1600 grid cells. Towards the wall, the mesh is refined six times. Each refinement divides a grid cell into four, giving a smallest grid size of 50 nm. As an initial condition for α, the droplet is assumed to be a perfect sphere, with its center of mass located at a height of 4.5 mm above the surface. To reach faster convergence of the gas velocity field, Stokes flow is assumed both inside and outside the droplet as the initial condition, and stresses are matched on the interface [28]. The pressure field does not need to be initialized and develops as the simulation progresses. Once the droplet is sufficiently close to the wall, the simulation results in the lower part of the large simulation box are saved and reinitialized within a small box of 1×0.5 mm with a resolution of 320×160 grid cells, which again gets refined towards the wall. The results presented in this paper are from simulations at two different refinement levels. To capture the details at the contact line and to capture splashing, it is sufficient to refine the mesh eight times at the wall, for a minimum grid size of about 12 nm. From a computational point of view, this is the smallest feasible mesh size that we can adopt for this system to run the simulations long enough to observe splashing. A second set of simulations focuses only on very early times. Because they run for a much shorter time it is possible to refine the mesh ten times and obtain an even higher resolution of about 3 nm. Complete convergence at the contact line would require a grid size below the slip length, which is approximately 1 nm and is beyond the reach of our computational resources. Nevertheless, at grid sizes of 3 and 12 nm the necessary physics of splashing are already present, and we expect the main observations of our simulations to be qualitatively correct. The width of both boxes is chosen to be large enough for the splash to occur within their confines.

For the simulations of a full splash, the impact velocity is $v_0 = 10.0$ ms^{-1} and the fluids are ethanol, for the liquid phase, and air, for the gas phase. This combination has been used in experiments [2], and has the advantage of showing an early splash, i.e., one that occurs shortly after impact. In experiments, the pressure effect is observed at moderately reduced gas pressures [2]. We therefore assume the dynamic viscosity of the air to be constant [29], but the density and the kinematic viscosity are allowed to change as pressure is reduced [29]. The reduced ambient pressure used in the simulations was deliberately chosen to be significantly lower than the experimentally observed threshold pressure, to ensure that the simulations were performed well into the suppressed splashing regime.

The impact velocities for the simulations resolving the early-time scales are $v_0 = 2.5$, 5.0, and 10.0 ms^{-1}. The liquid viscosity is either the viscosity of ethanol or ten times that of ethanol and the surface tension is either the normal surface tension between air and ethanol or 20 times this surface tension, which is of the same order as the surface tension of mercury in air. In order to keep memory requirements within the constraints of our infrastructure, we consider a two-dimensional axisymmetric droplet with a diameter of 300 μm (as opposed to the 3-mm droplets used in experiments [2]).

III. RESULTS

A. Overview

To provide a context for the next sections on the behavior of the gas film under the droplet and lamella ejection, in this section an overview is given of how the simulations reproduce the pressure effect. Figure 1 shows a time series of the pressure effect for a droplet approaching the surface

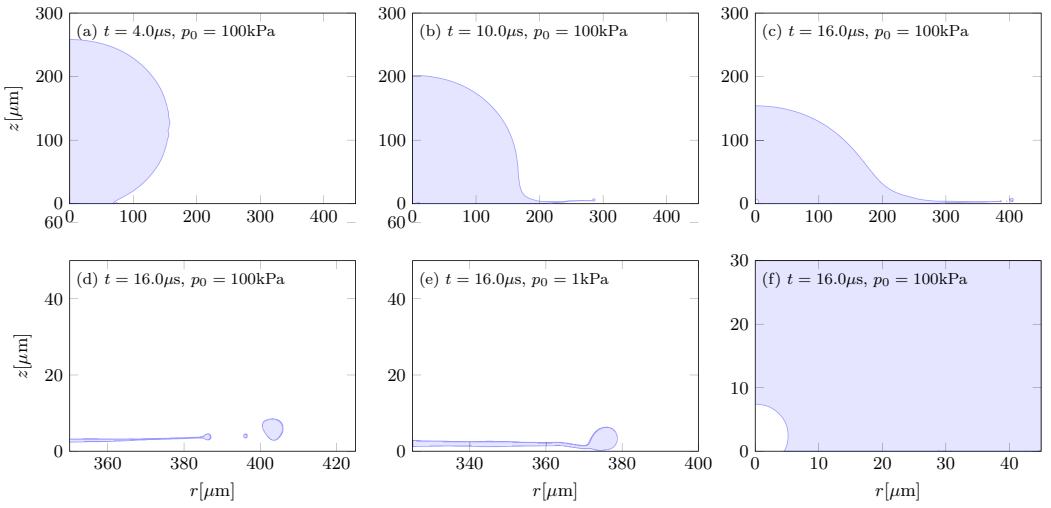

FIG. 1. Time series of the impact of a droplet on a dry surface. The top frames (a)–(c) show simulation results for atmospheric pressure at different times. The bottom frames show (d) liquid-sheet breakup at atmospheric pressure, (e) no breakup at reduced pressure, and (f) the central air bubble.

at $v_0 = 10$ ms^{-1}. The top half shows three images of droplet impact and liquid-sheet ejection on a completely wetting surface at ambient pressure $p_0 = 100$ kPa. The first frame, Fig. 1(a), shows the droplet right after impact. As the droplet approaches the wall, gas pressure builds up at the stagnation point to about $p = 1200$ kPa. This causes the droplet to deform, and a gas film in the shape of a spherical dome to appear underneath it. As the gas film becomes thinner, air gets squeezed out and reaches velocities of up to $|\vec{v}| = 150$ ms^{-1}. When the liquid eventually touches the wall, a small amount of air is permanently trapped, forming the central air bubble with a diameter of about $d = 10$ μm [8,10,11]. This bubble can be seen in Fig. 1(f).

Right after impact a liquid sheet is ejected with a velocity of approximately $v_e = 100$ ms^{-1}. The liquid sheet forms at both atmospheric, $p = 100$ kPa, and reduced pressure, $p_0 = 1$ kPa. However, at atmospheric pressure the sheet gets lifted and breaks up into smaller droplets; in contrast, at reduced pressure it stays close to the surface and remains intact. Figure 1(c) shows the liquid sheet as it breaks up into smaller droplets at atmospheric pressure. Figure 1(d) shows a magnified image of the liquid sheet as it breaks up. The droplet that breaks off has a diameter of $d = 7$ μm. Figure 1(e) shows a snapshot taken at the same time, but at a reduced pressure. One can see that instead of breaking up, the liquid sheet stays in one piece: Splashing is suppressed by decreasing the ambient pressure.

The reason simulations are useful to investigate the gas film behavior and liquid-sheet ejection is that they provide access to length and timescales that are not easily observed in experiments. This feature is illustrated in Fig. 2, which presents a magnified time series of the liquid/gas interface at the contact line. A blue color corresponds to the liquid phase and white to the gas phase. These snapshots are taken at atmospheric pressure, from the moment just after impact until the point when the edge of the droplet is about to leave the simulation box. Drop impact is defined as the moment that a droplet would have hit the surface, continuing its trajectory instead of spreading on a gas film. This occurs at $t = 6.2$ μs. Figure 2(a) shows the contact line just after impact and right before a liquid sheet forms at $t = 6.25$ μs. Once the liquid sheet forms, which can be seen in Fig. 2(b), it is ejected right away. A feature revealed by experiments [8] is contact-line dewetting. At high speeds the interface in front of the contact line becomes unstable and touches down on the surface, causing gas bubble entrainment at the contact line. This phenomenon can be appreciated in Fig. 2(c), which at $r \approx 168$ μm shows a gas bubble that formed when the contact line became unstable, and the liquid in front of the contact line touched down on the surface. The first touchdown event is observed

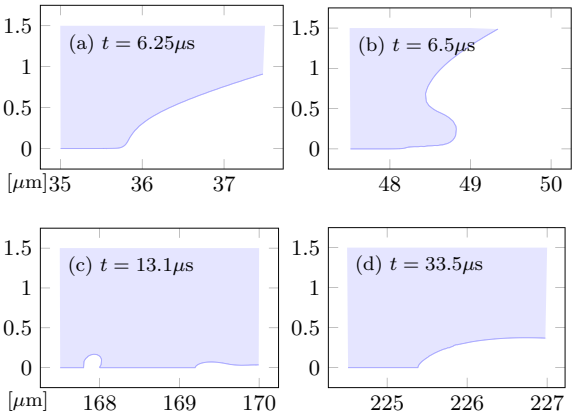

FIG. 2. Time series of the droplet interface showing the evolution of the contact line at atmospheric pressure. Light blue represents the liquid phase. The vertical axis shows the distance normal to the surface and the horizontal axis shows the distance parallel to the surface relative to the center of the droplet. Both axes are in μm.

at $t = 7.33$ μs, and at $t = 14.4$ μs the contact line stabilizes again. Figures 2(c) and 2(d) are well within the unstable and stable contact-line regimes, respectively.

Resolving the ejection of this same lamella in an experiment with a high-speed camera would call for the following specifications: Considering a deacceleration of about -4.0×10^7 ms^{-2} right after ejection, to capture a velocity difference of 8 ms^{-1}, 10% of the ejection velocity, one would need to capture one frame every 0.2 μs. This corresponds to a frame rate of 5.000.000 frames per second. To resolve a lamella thickness of 0.5 μm with 10 pixels, a resolution of 0.05 μm per pixel is needed. Methods such as total internal reflection (TIR) [19] and interference [15] can achieve very high spatial and temporal accuracy. However, only a very small part of the droplet interface can be studied, while simulations show the complete interface, including the gas film and the lamella.

B. Gas film

This section looks in more detail at the gas film which forms under the droplet upon impact. The evolution of the gas film for various parameters is shown in Fig. 3. The vertical axis shows the height away from the wall and the horizontal axis the radial distance away from the center. Both axes are in μm. The figures in the top row show an impact velocity of 2.5 ms^{-1} and the time difference between successive lines is 1.0 μs. The figures in the bottom row show the gas film for an impact velocity of 10.0 ms^{-1} with a time difference of 0.1 μs between successive lines. Figures 3(a) and 3(e) show the gas film for ethanol at atmospheric ambient pressure, Figs. 3(b) and 3(f) show the results for the high-viscosity liquid (i.e., a viscosity ten times higher than the viscosity of ethanol), Figs. 3(c) and 3(g) show the results for the liquid with a high surface tension (i.e., a surface tension 20 times higher than the surface tension of ethanol in air), and Figs. 3(d) and 3(h) show the results for ethanol at reduced ambient pressure (i.e., an ambient pressure 1/100 of atmospheric pressure). Comparing the top and bottom row shows that a higher impact velocity results in a thinner gas film. The fluctuations of the interface close to the wall in the bottom row are the result of the gas film collapsing behind the edge of the spreading droplet. Comparing Figs. 3(a) and 3(b) shows that for early times a higher viscosity results in a thicker gas film. Both the effect of velocity and viscosity are consistent with literature [19]. An increased surface tension also gives an increased gas film thickness while a lower ambient pressure has little effect on the thickness of the gas film.

A more quantitative representation of the gas film height can be seen in Fig. 4. This figure shows the height of the gas film at the edge of the droplet in nm at the moment of lamella formation as

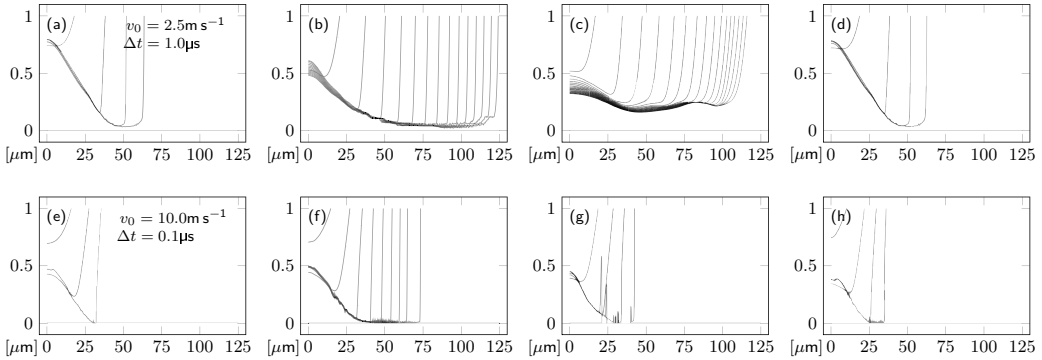

FIG. 3. Gas film profiles of different droplets approaching the wall. The vertical axis shows the height above the wall and the horizontal axis the radial distance away from the center. Both axes are in μm. The figures in the top row (a)–(d) show an impact velocity of 2.5 ms^{-1} and the time difference between successive lines is 1.0 μs. The figures in the bottom row (e)–(h) show an impact velocity of 10.0 ms^{-1} with a time difference of 0.1 μs. (a) and (e) show the results for ethanol at atmospheric ambient pressure, (b) and (f) show the results for the high-viscosity liquid (i.e., a viscosity ten times higher than the viscosity of ethanol), (c) and (g) show the results for the liquid with a high surface tension (i.e., a surface tension 20 times higher than the surface tension of ethanol in air), and (d) and (h) show the results for ethanol at reduced ambient pressure (i.e., an ambient pressure 1/100 of atmospheric pressure).

a function of impact velocity. The observations made above for an impact velocity of 2.5 ms^{-1} concerning the effect of viscosity, surface tension, and pressure on the thickness of the gas film are shown to also hold for higher impact velocities. Moreover, a higher impact velocity can be seen to reduce the thickness of the gas film irrespective of the liquid properties of the droplet or the ambient gas pressure. In addition to the various data points, Fig. 4 also shows a prediction by Mandre and Brenner [11] for the thickness of the gas film as a function of impact velocity. They propose a scaling of $z_f = 60 r_0\,\mathrm{St}^{4/3}$, where $\mathrm{St} = \mu_g/(\rho_l v_0 r_0)$ is the Stokes number, r_0 is the radius of the droplet, ρ_l is the liquid density, and μ_g is the gas viscosity. While the prefactor is different, possibly due to differences in geometry and the fact that the theory was developed for inviscid flow, the scaling is consistent with theory.

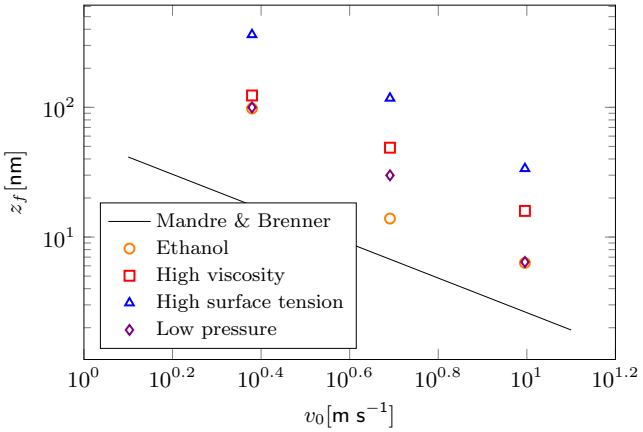

FIG. 4. Height of the gas film under the drop at the moment of lamella formation for various velocities, viscosities, and surface tensions. The line shows the theoretical predictions by Mandre and Brenner [11].

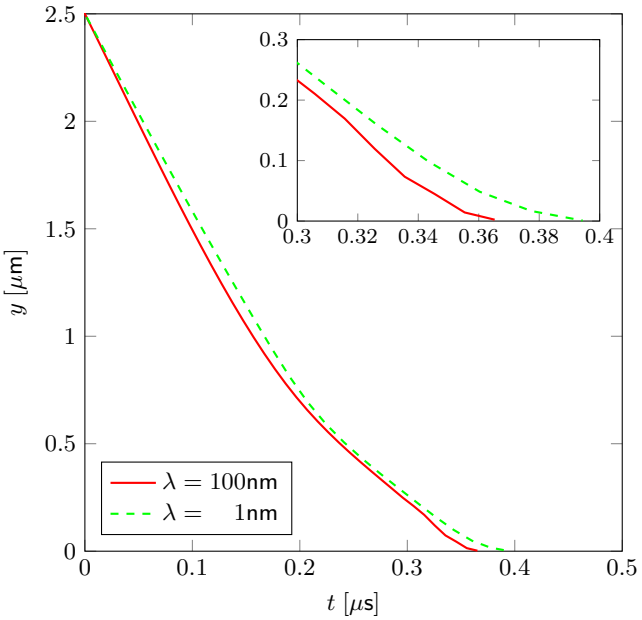

FIG. 5. The minimum thickness of the gas film as function of time comparing two simulations: one simulation with a slip length of $\lambda = 1$ nm, and one simulation with a slip length of $\lambda = 100$ nm. Both simulations are performed at reduced ambient pressure. The inset shows a magnified view of the droplets approaching the wall.

One aspect of the figure that needs to be examined more closely is that fact that, especially at higher impact velocities, the thickness of the gas film under the droplet upon impact becomes very thin. Considering that at room temperature and atmospheric pressure the mean free path is around $\lambda \approx 70$ nm [30], this suggests that the continuity assumption is not valid and raises the question how a breakdown of the continuity assumption would affect the simulation results. Mandre and Brenner [11] show that at larger impact velocities the continuum assumption breaks down and they predict that this leads to an earlier rupture of the gas film. The effect of the breakdown of continuity can be modeled by increasing the slip length on the wall [20]. Figure 5 shows the minimum thickness of the gas film as a function of time comparing slip lengths of 1 and 100 nm. Both simulations are of an ethanol droplet falling through air at reduced ambient pressure. The simulation results are only shown until right before collapse of the gas film. The code supports only one slip length, and as mentioned in the Theory and Methods section, the slip length of $\lambda = 1$ nm was chosen because it is a good value for the contact line. The slip length of $\lambda = 100$ nm was chosen because the slip length is inversely proportional to pressure [20] and the ambient pressure was reduced a hundredfold. It can be appreciated that the increased slip length does result in a slightly earlier collapse of the gas film, consistent with literature [11]. In addition, it has been reported that at atmospheric ambient pressure, the maximum contact-line velocity is not greatly affected by the presence of a slip boundary condition for the gas phase [20]. This suggests that although the gas film is expected to collapse sooner when the continuum assumption breaks down, there should be a gas film present at the edge of the spreading droplet.

As mentioned in the Introduction, apart from the gas film forming under the droplet upon impact, there is also a gas film under the liquid sheet. To be able to analyze the thickness of this gas film, Fig. 6 shows a time series of the contour of the droplet at atmospheric pressure with the vertical axis plotted on a logarithmic scale. Since the vertical axis cannot go to zero, it is cut off at 10^{-3} μm, and the center of the drop corresponds to the vertical axis. Figure 6(a) shows the droplet right after

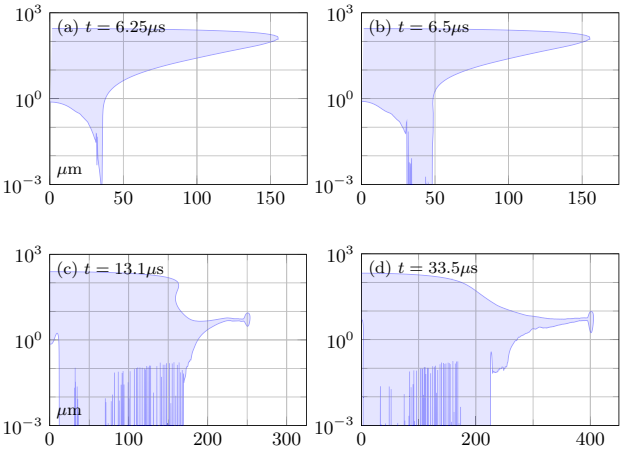

FIG. 6. Time series of the droplet interface with the vertical axis plotted on a logarithmic scale. The axis are in μm and the vertical axis is plotted on a logarithmic scale. Since the vertical axis cannot go to zero, it is cut off at 10^{-3} μm.

impact with the central air dome clearly visible. Initially, the bubble is slightly under 1 μm high, and about 30 μm wide. The vertical lines or peaks under the droplet are small air bubbles which were trapped on impact. The next figure shows the droplet right after a liquid sheet is ejected and the third frame shows the droplet in the unstable contact-line regime. The vertical lines behind the contact line are small air bubbles which were entrained by the moving contact line. Also, it can be observed how the contact line of the central air bubble is moving toward the center. The gas layer under the liquid sheet is on the order of several microns thick. The last figure, Fig. 6(d), shows the droplet with a stable contact line. There are no longer droplets being trapped right behind the contact line. Instead, there is just one cavity present at the contact line with a height of a little under 1 μm. The gas film right after the cavity has a thickness of about 0.1 μm, and increases again to several microns towards the rim of the liquid sheet.

To put the above numbers in perspective, they need to be compared to the mean free path of air. At room temperature and atmospheric pressure the mean free path is around $\lambda \approx 70$ nm [30]. The typical thickness of the gas layer is several microns, so the continuity approximation should be valid for these simulations. Since the mean free path scales with the kinematic viscosity, at the reduced pressure the mean free path is about $\lambda \approx 7$ μm, which is about the same height as the typical thickness of the gas layer. This means that at reduced pressure the validity of the continuum approximation is pushed to its limits, and that the simulations may slightly overestimate the longevity of the gas film under the liquid sheet at reduced pressure. Additionally, at reduced ambient pressure the maximum velocity of the contact line is expected to increase [20]. If the liquid sheet is not ejected fast enough, this might affect the simulation results.

Having addressed the issue of continuum assumption breakdown, an important consequence of the existence of a thin gas film under the droplet can now be discussed. Due to the semilogarithmic scaling of Fig. 6, the contact line is difficult to see, but in Fig. 7 a magnified time series of the contact line and corresponding streamlines are shown at atmospheric pressure. Figure 8 shows the contact line and corresponding vorticity contour plot $\omega = \nabla \times \vec{v}$ at the same magnification. While in the last two frames of both figures a normal low-speed contact line can be observed, the first two frames show a strongly curved interface, which continues under the droplet. To gain more insight into the behavior of the curved interface at the contact line, we now focus on the streamlines in Fig. 7. It can be appreciated that in the first two frames, for a length of about 0.1 μm along the wall, a fluid parcel starting at the interface will closely approach the wall when tracing its streamline. This behavior is

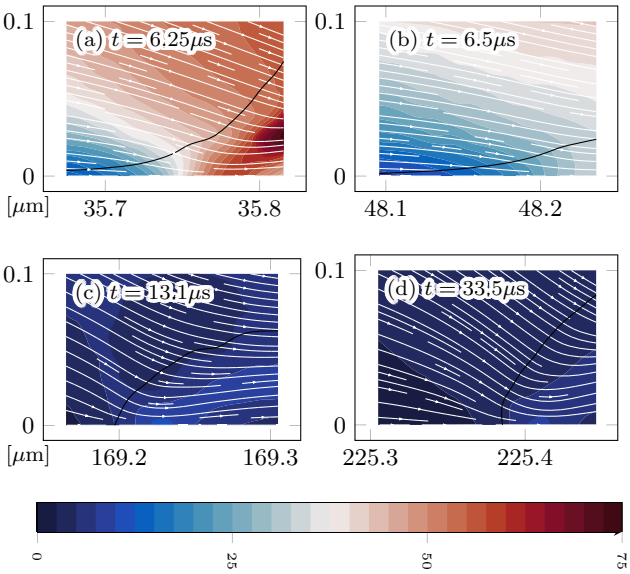

FIG. 7. Time series of the droplet interface, velocity magnitude, and streamlines, showing the evolution of the contact line at atmospheric pressure. This time series is magnified 15 times compared to Fig. 2. The velocity magnitude is in ms^{-1}, and the axes are in μm. The small arrows on the streamlines indicate the direction of the flow.

reminiscent of the interface rolling over the surface at a high speed, as a caterpillar track. The lower two frames show a traditional sliding contact line and the area where a fluid parcel would end up at the wall is much smaller. Looking at the vorticity contours in Fig. 8, a very strong negative vorticity can be observed at the wall in the top two frames. This suggests that in this area fluid parcels have a strong tendency to rotate clockwise as they move along their streamlines, again suggesting the presence of a rolling motion. The presence of a rolling contact-line regime seems to be crucial to splashing. Coarsening the resolution just enough so that the gas film at the edge of the drop and the rolling contact line do not get resolved, prevents a droplet from splashing on impact. It has been brought to our attention that the rolling contact-line regime recently also has been observed in another publication [31].

C. Lamella

Just as the previous section looked into the effect of various material properties on the formation of a gas film under the droplet, this section looks at the effect of these same parameters on lamella formation. Figure 9 shows various time series of droplets with impact velocities of 2.5 ms^{-1} (top row) and 10.0 ms^{-1} (bottom row). Figures 9(a) and 9(e) show ethanol droplets at atmospheric ambient pressure, Figs. 9(b) and 9(f) show the droplets with a high viscosity of ten times the viscosity of ethanol, Figs. 9(c) and 9(g) show the droplets with a high surface tension of a fluid with 20 times the surface tension of ethanol in air, and Figs. 9(d) and 9(h) show the evolution of ethanol droplets at an ambient pressure reduced 100 times compared to atmospheric pressure. The droplets are shown until the moment of lamella formation. It can be seen that a higher impact velocity results in a thinner lamella which forms earlier. In addition, it can be observed that both increased viscosity and surface tension result in a thicker lamella, which is ejected later. Pressure, on the other hand, does not have an effect on the moment of lamella ejection.

In Fig. 10 the simulation data are shown in a more quantitative form. Figure 10(a) shows the height of the lamella z_e at the moment of ejection as a function of the time since impact t on a log-log

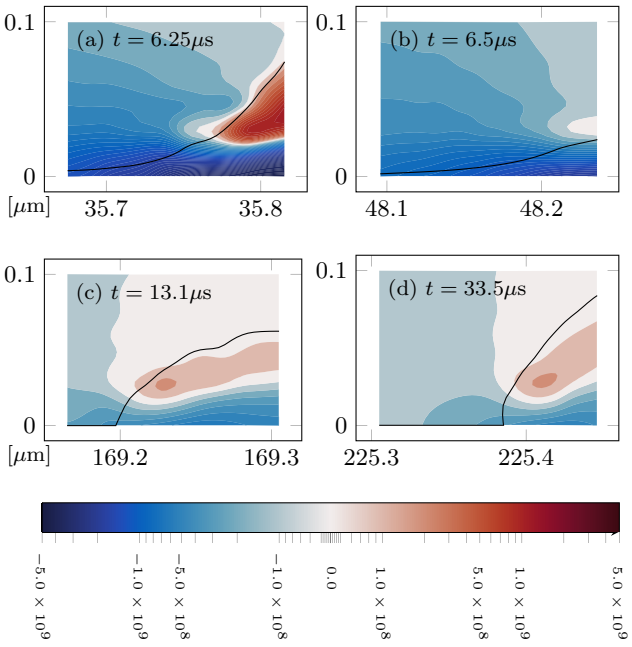

FIG. 8. Time series of the droplet interface and vorticity ω showing the evolution of the contact line at atmospheric pressure. This time series is magnified 15 times compared to Fig. 2. The axes are in μm and the contours in s^{-1}.

plot. The data are shown for a droplet of ethanol in both atmospheric and reduced ambient pressure, a high-viscosity droplet, and a high surface-tension droplet. The impact velocities are 2.5, 5.0, and 10.0 ms^{-1}. A higher impact velocity results in an earlier ejection time. An earlier ejection time, in turn, results in a thinner lamella. Increasing the surface tension and viscosity delays the moment of lamella ejection, resulting in a thicker lamella. In Fig. 10(b) the lamella ejection velocity as a

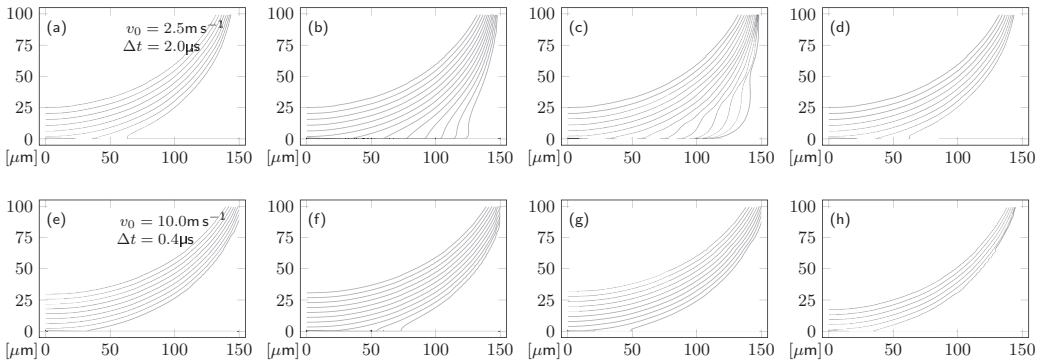

FIG. 9. Lamella profiles of different droplets approaching the wall. The vertical axis shows the height above the wall and the horizontal axis the radial distance away from the center. Both axes are in μm. The figures in the top row (a)–(d) show an impact velocity of 2.5 ms^{-1} and the time difference between successive lines is 2.0 μs. The figures in the bottom row (e)–(h) show an impact velocity of 10.0 ms^{-1} with a time difference of 0.4 μs. (a) and (e) show the results for ethanol at atmospheric ambient pressure, (b) and (f) show the results for the high-viscosity liquid (i.e., ten times higher than the viscosity of ethanol), (c) and (g) show the results for the liquid with a high surface tension (i.e., 20 times higher than the surface tension of ethanol in air), and (d) and (h) show the results for ethanol at reduced ambient pressure (i.e., 1/100 of atmospheric ambient pressure).

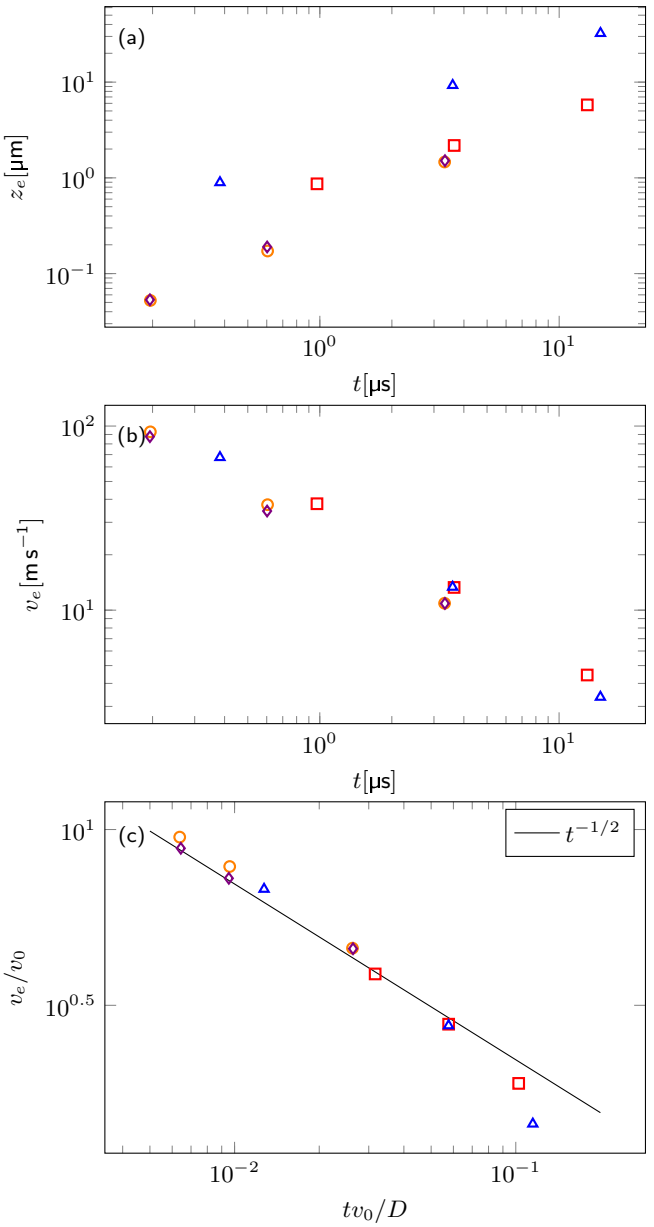

FIG. 10. Various lamella properties as a function of its ejection time. In all three plots the results are shown for an ethanol droplet in a gas at atmospheric ambient pressure (○), and ethanol drop in a gas at reduced ambient pressure (◇), a droplet with a high surface tension in a gas at atmospheric ambient pressure (△), and a droplet with a high viscosity (□). (a) Lamella height z_e as a function of ejection time t_e. The three data points per symbol correspond to impact velocities of 2.5, 5.0, and 10.0 ms^{-1} with 10.0 ms^{-1} resulting in the smallest ejection time. (b) Lamella ejection velocity v_e as a function of ejection time t_e. The ejection velocity can be nondimensionalized using the impact velocity v_0 and droplet diameter D, the result of which can be seen in (c). The data follow a scaling of $v_e/v_0 \propto t^{-1/2}$.

function of ejection time can be seen. For all the different liquid properties a later ejection time gives a lower ejection velocity. In addition, when the data are nondimensionalized with the impact velocity

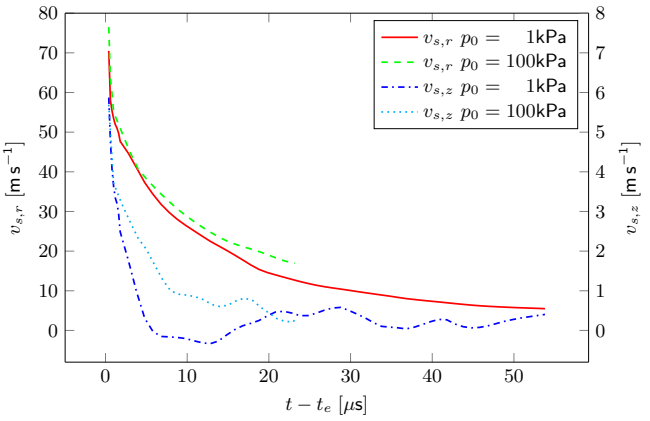

FIG. 11. The radial and vertical velocity of the liquid sheets ejected from the droplet as a function of time. t_e is defined as the moment of sheet ejection.

v_0 and droplet diameter D, the data collapse to a single line with an exponent of $v_e/v_0 \propto t^{-1/2}$. For especially the last point, a deviation from this scaling can be observed. The reason for this can be seen in Fig. 9(c). At the impact velocity of 2.5 ms^{-1} the increased surface tension slows down ejection time by so much that the lamella size can no longer be considered to be much smaller than the droplet size, $z_e \not\ll D$, which results in different dynamics for lamella formation.

Simulations can also also provide insight on how the velocity of the lamella evolves after ejection as it gets lifted up and becomes a liquid sheet. Two simulations were continued after lamella formation. In both simulations the droplet has an impact velocity of $v_0 = 10$ ms^{-1}, but one simulation is at atmospheric ambient gas pressure and one is at reduced ambient gas pressure. The results are shown in Fig. 11. The left axis shows the radial liquid-sheet velocity while the right axis shows the vertical liquid-sheet velocity. The velocity curves for the simulation at atmospheric ambient pressure end when the liquid sheet breaks up. In this graph, $t = 0$ is the moment of liquid-sheet ejection t_e, which is defined as the moment a local maximum can first be detected in the width of the droplet close to the wall. This local maximum is the beginning of a lamella. It can be appreciated that both the initial vertical and horizontal ejection velocities are very similar between the normal and reduced pressure cases. This is expected because lamella ejection occurs very shortly after impact, and the impact dynamics is typically described by the Reynolds number and the Weber number [6], neither of which depend on the properties of the ambient gas. Only at later times do the velocities start to differ, resulting in the liquid sheet at atmospheric ambient pressure being lifted higher than the liquid sheet at reduced ambient pressure, resulting in its breakup.

IV. DISCUSSION

While in this section various splashing and droplet-deposition models are discussed, the reproduction of the pressure effect in our simulations in itself leads to important conclusions. To reduce the number of variables, both the liquid and gas phases are assumed to be incompressible; this indicates that a shock wave cannot be solely responsible for liquid-sheet formation [8]. Also, vortex formation in the gas phase upon impact is not necessary for splashing [32]. Although the vortices are not resolved in our simulations, the effect of pressure is still captured. Lastly, the breakup of the liquid sheet is thought to be caused by either a Plateau-Rayleigh instability, or a Rayleigh-Taylor instability [33]. Although a Plateau-Rayleigh instability can play a role in three-dimensional splashing, since in these two-dimensional simulations breakup is still observed, it can be concluded that such an instability is not a necessary condition to observe splashing.

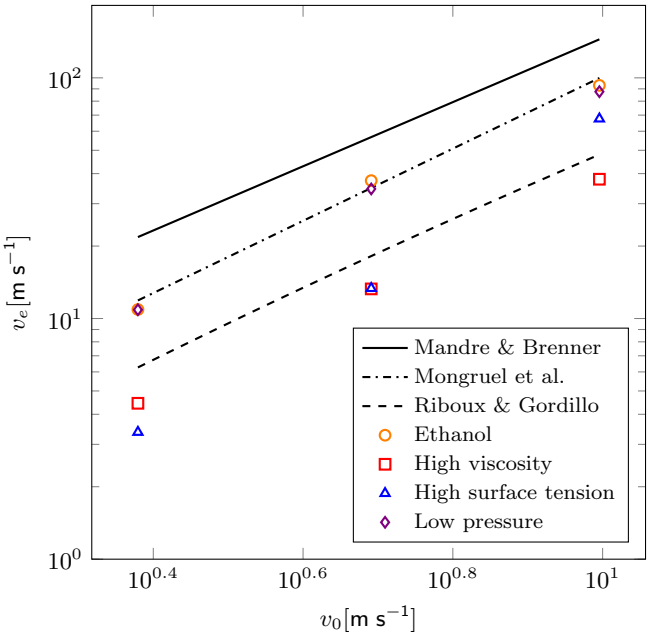

FIG. 12. Lamella ejection velocity as function of the impact velocity of a droplet for various velocities, viscosities, and surface tensions. Ethanol refers to the simulations of ethanol in air, "high viscosity" refers to simulations of a fluid with ten times the viscosity of ethanol in air, and "high surface tension" refers to simulations of a fluid with 20 times the surface tension of ethanol in air. The lines show theoretical predictions by Mandre and Brenner [11] ($v_e \propto v_0^{4/3}$), Riboux and Gordillo [17] ($v_e \propto v_0^{1.3}$ in the current regime), and Mongruel *et al.* [18] ($v_e \propto v_0^{3/2}$). The error bars in this figure are smaller than the symbols.

To illustrate the need to perform a detailed comparison between the various existing models for splashing, in Fig. 12 the ejection velocity v_e is plotted as a function of impact velocity v_0. The correct prediction of the ejection velocity is important, because it an essential part of predicting splashing behavior [17]. The impact velocity is chosen here as the independent variable instead of time because different models have different definitions for the time of impact, which becomes relevant when ejection time occurs very shortly after impact. As was seen in Fig. 10, it can be observed that reducing the ambient pressure does not have much of an effect on lamella formation. However, both an increased viscosity and an increased surface tension significantly reduce the ejection velocity. In addition to the simulation data, the graph shows theoretical curves corresponding to predictions for ethanol drops in air. The formulas are shown in the different sections below. To plot the theoretical curves of Mandre and Brenner [11] and Riboux and Gordillo [17], the prefactors that are provided with their respective theories are used. Since Mongruel *et al.* [18] do not provide a prefactor, a prefactor of 0.275 was chosen to match the data. To be able to clearly observe the differences in scaling of the liquid-sheet ejection velocity as a function of the impact velocity, velocities are not nondimensionalized.

It can be seen in this graph that different theories all predict a similar scaling relation for the lamella ejection velocity as a function of the impact velocity. This makes it difficult to distinguish between these different theories in both experiments and simulations, and in the following sections a more fundamental look is taken at the assumptions that underlie each theory.

To begin with, the relevant nondimensional numbers of the system are given here,

$$\mathrm{St} = \frac{\mu_g}{\rho_l v_0 r_0}, \quad \mathrm{We} = \frac{\rho_l v_0^2 r_0}{\sigma}, \quad \mathrm{Re} = \frac{\rho_l v_0 r_0}{\mu_l}, \quad \text{and} \quad \mathrm{Oh} = \frac{\sqrt{\mathrm{We}}}{\mathrm{Re}},$$

where St is the inverse Stokes number, Re is the Reynolds number, We is the Weber number, and Oh is the Ohnesorge number. These numbers have the values $\mathrm{St} = 1.3 \times 10^{-5}$, $\mathrm{We} = 528$, $\mathrm{Re} = 986$, and $\mathrm{Oh} = 2.33 \times 10^{-2}$, which were calculated using the following parameters: $v_0 = 10\ \mathrm{ms}^{-1}$, $\rho_l = 789\ \mathrm{kg\,m}^{-3}$, $\mu_l = 1.20 \times 10^{-3}\ \mathrm{Pa\,s}$, $\rho_g = 0.01\ \mathrm{kg\,m}^{-3}$ at $p_0 = 1\ \mathrm{kPa}$, $\rho_g = 1.00\ \mathrm{kg\,m}^{-3}$ at $p_0 = 100\ \mathrm{kPa}$, $\mu_g = 1.48 \times 10^{-5}\ \mathrm{Pa\,s}$, $\sigma = 0.022\,39\ \mathrm{J\,m}^{-2}$, and $r_0 = 150\ \mu\mathrm{m}$. These numbers suggest that in our simulations impact is dominated by the inertia of the fluid.

A. Dewetting

In this section, the dewetting model by Riboux and Gordillo [17] is further investigated. Key assumptions of this model are that the liquid moves fast enough so that the formation of a gas film under a liquid sheet is caused by the liquid dewetting the surface. However, this is not consistent with the results of the simulations. As shown in the results, instead of dewetting, a rolling contact line is observed. While the gas film under the droplet can collapse, the edge of the droplet never touches the surface. Consistent with literature [34], the existence of the gas film seems essential for splashing. Liquid-sheet formation is suppressed when the gas film is not resolved in our simulations. In addition, while this needs to be investigated further, the simulations with different slip lengths hint at the possibility that at reduced ambient pressure the slip length can become so large that the formation of the gas film is suppressed [20]. This is also observed in experiments [8].

Since droplet deposition is dominated by inertia and not by contact-line dissipation [35], independent of the argument of how a gas film forms under the liquid sheet, one can investigate the model's predictions for lamella formation and liquid-sheet breakup. The theory states that a lamella will be ejected when the acceleration of a material point in the lamella is larger than the acceleration of the spreading radius of the drop. This acceleration is determined by a balance between inertial, viscous, and capillary forces, leading to an ejection time prediction,

$$c_1\,\mathrm{Re}^{-1} t_{e,R}^{-1/2} + \mathrm{Re}^{-2}\,\mathrm{Oh}^{-2} = c^2 t_{e,R}^{3/2}. \tag{8}$$

Here, $t_{e,R}$ is the sheet ejection time, nondimensionalized with the impact velocity v_0 and the droplet radius r_0, and c_1 and c are two constants with the values $c_1 = \sqrt{3}/2$ and $c = 1.1$. Using the ejection time, the ejection velocity can be calculated with the equation

$$v_{e,R} = \frac{\sqrt{3}}{2} t_{e,R}^{-1/2}. \tag{9}$$

The above equation is used to calculate the lamella ejection velocity in Fig. 12. As was mentioned above, although the scaling of the ejection velocity as a function of the impact velocity is consistent with our data, the provided fitting parameters do not fit our data well. This could be explained by the fact that the experiments that were used to fit their model did not have access to the time and length scales that these simulations can capture. Since the velocity of a lamella changes rapidly after ejection, this can lead to a significant error. However, even after fitting the model to our simulation data for an ethanol droplet, we find that it correctly predicts the effect of surface tension, but not the effect of viscosity.

After lamella formation the dewetting model predicts that a drop will or will not splash based on whether a lift force is able to lift up the liquid sheet into the air, causing the drop to splash, or whether it rewets the surface. This results in the definition of a parameter $\beta = v_{h_t,z}/v_{\mathrm{tc}}$, where $v_{h_t,z}$ is the vertical velocity of the liquid sheet when it has risen to a characteristic height of h_t, and v_{tc} is the Taylor-Culick velocity. In this paper, two different methods to calculate β are used; based on material properties and impact conditions, Riboux and Gordillo [17] provide a theoretical prediction for the value of $v_{h_t,z}$. When this theoretical value is used, β is called β_R and it is calculated using the equation

$$\beta_R = \left(\frac{K_l \mu_g (v_{e,R} v_0) + K_u \rho_g (v_{e,R} v_0)^2 (h_t r_0)}{2\sigma} \right)^{1/2}, \tag{10}$$

TABLE I. Comparison of simulation results with predictions of the model by Riboux and Gordillo [17] for two different ambient pressures. The table shows the ejection velocities, and the splashing criterion of the liquid sheet. v_e and β_S are simulation results. $v_{e,R}$ and β_R are the predictions by Riboux and Gordillo.

P_0 (kPa)	$v_{e,R}$	v_e	β_R	β_S
1	4.87	7.05	0.075	0.523
100	4.87	7.65	0.649	0.557

with

$$K_l = -\frac{6}{\tan^2(\alpha)}\left[\ln\left(16\frac{l_g}{h_t r_0}\right) - \ln\left(1 + 16\frac{l_g}{h_t r_0}\right)\right], \tag{11}$$

and

$$K_u = 0.3. \tag{12}$$

In the above equation $\alpha = 20/180\pi^\circ$, and $l_g = 1.2\lambda$, the slip length of the gas. $\lambda = \lambda_0(p_{\text{atm}}/p_0)$ with $\lambda_0 = 65$ nm the mean free path of air at room temperature and atmospheric pressure $p_{\text{atm}} = 100$ kPa. However, $v_{h_t,z}$ can also be directly determined from the simulation data, in which case β is called β_S and is calculated from our simulations using

$$\beta_S = \frac{v_{h_t,z} v_0}{\sqrt{2\sigma/(\rho_l h_t r_0)}}, \tag{13}$$

where $v_{h_t,z}$ is the vertical velocity of the liquid sheet when it has risen to a characteristic height of

$$h_t = \frac{\sqrt{12}}{\pi} t_{e,R}^{3/2}. \tag{14}$$

For $p_0 = 1$ kPa this is the vertical velocity at $t = 0.17$, and for $p_0 = 100$ kPa at $t = 0.26$.

In Table I the theoretical predictions of Riboux and Gordillo [17] are shown. The theoretically predicted values for β are $\beta_R = 0.075$ and $\beta_R = 0.649$ for calculations at $p_0 = 1$ and 100 kPa, respectively. However, the values calculated from the simulations are $\beta_S = 0.523$ and $\beta_S = 0.557$. Comparing β_S and β_R shows that theory predicts about an order of magnitude difference between the normal and reduced pressure cases. However, the values calculated from the simulations show similar values of β for both normal and reduced pressures. This suggests that when using the definition in Eq. (13), β is not able to predict splashing for these simulations. However, the vertical velocity components, shown in Fig. 11, do suggest that a lift force could be responsible for the breakup of a liquid sheet. Consistent with Eqs. (8) and (9), the lamella ejection time and velocity are independent of pressure. Only at later times, when a lift force could have started to act on the liquid sheet, do the velocities start to differ, supporting the lift force hypothesis. In addition, the existence of a lift force would explain why, although there is a strong vertical component to the liquid-sheet velocity in Fig. 11, the liquid sheet does not rise as high as is typically seen in experiments. The droplet size used in these simulations is much smaller than a typical droplet used in experiments resulting in a smaller liquid sheet and thus smaller lift force.

While the dewetting theory is able to correctly predict splashing for a large number of experiments [17,36], the theory's predictions do not match well with the simulations presented in this paper. This includes the dewetting assumption for the formation of the gas film, the model for lamella formation, and the splashing criterion. A possible explanation for the mismatch between the simulations and theory is that the experiments that were used to benchmark the fitting parameters in the theory could not have measured liquid-sheet velocities at the early times observed in our simulations. Another major difference with comparisons where the dewetting theory gives good predictions for lamella formation and splashing is that the typical droplet size in these experiments is on the order of mm while the droplets in this paper are significantly smaller. Visser *et al.* [37] also find that the dewetting

model does not correctly predict splashing for their microdroplets and attribute this to violating the assumption that the air film thickness under the liquid sheet exceeds the mean free path length of the gas molecules. However, as shown above, in this paper, at atmospheric pressure the gas film under the liquid sheet is thicker than the mean free path of the gas molecules, which leaves open the question whether there are other size effects at play.

B. Skating

This section focuses on the skating droplet theory of Mandre and Brenner [11]. As shown in Sec. III B, the simulation data are consistent with the basic assumption of the skating model that the droplet moves on top of a very thin gas film upon impact. While this gas film can collapse with time, when a liquid sheet forms, the edge of the droplet never touches the surface. The thin gas film has also been observed in recent experiments, both directly [38] and indirectly [34]. In addition, the simulation results are consistent with the proposed scaling of the nondimensional gas film height,

$$z_f = 60\,\mathrm{St}^{4/3}, \tag{15}$$

where $\mathrm{St} = \mu_g/(\rho_l v_0 r_0)$ is the Stokes number, r_0 is the radius of the droplet, ρ_l is the liquid density, and μ_g is the gas viscosity. However, because the theory was developed for inviscid flow, it does not account for the effect of viscosity and surface tension. Also consistent with the theory, the gas film scaling does not depend on gas pressure. However, when in the simulations the slip length on the wall is increased, the gas film drains faster. Since the slip length depends on the ambient gas pressure [20], it would be interesting to perform a follow-up study with a wider range of slip lengths to study the effect of the breakdown of continuity on the gas film at low gas pressure.

The presence of the gas film and the introduction of a rolling contact line also provide a possible explanation for the recent experimental finding that splashing is independent of the wetting properties of the surface [39]. When the contact line is in the rolling regime, its contact angle is always 180°, and thus it should behave in exactly the same manner on wetting and nonwetting surfaces. Therefore, in this regime, liquid-sheet formation is predicted to be independent of the wetting properties of the surface.

The nondimensional lamella ejection velocity can be calculated with the following equation,

$$v_{e,M} = 0.34\,\mathrm{St}^{-1/3}, \tag{16}$$

where the liquid-sheet ejection velocity $v_{e,M}$ is nondimensionalized with the impact velocity v_0. As was shown in Fig. 12, the predicted scaling of the ejection velocity as a function of the impact velocity is consistent with the simulation results. However, the prefactor does not match, possibly due to geometry differences. Also, just as was the case for the scaling of the gas film height, the effects of viscosity and surface tension are not captured in this model.

In addition to scaling relations for the gas film and the lamella ejection velocity, Mandre and Brenner [11] propose the hypothesis that splashing is caused by liquid deflecting on the surface. If this were the case, one would expect different ejection velocity directions for a droplet impacting at atmospheric ambient pressure and at reduced ambient pressure. It can be observed in Fig. 11 that this is not consistent with the simulation data, and that thus our results suggest that deflection on the surface is not a valid splashing mechanism.

C. Lamella formation

In this last section, the model for lamella formation developed by Mongruel *et al.* [18] is discussed. As was shown in Fig. 12, the proposed scaling for the ejection velocity,

$$v_{e,N} \propto \sqrt{\mathrm{Re}}, \tag{17}$$

matches the simulation data well. In addition, this model predicts correctly that the ejection velocities for high-viscosity droplets are about $\sqrt{10}$ times lower than the ejection velocities for the normal

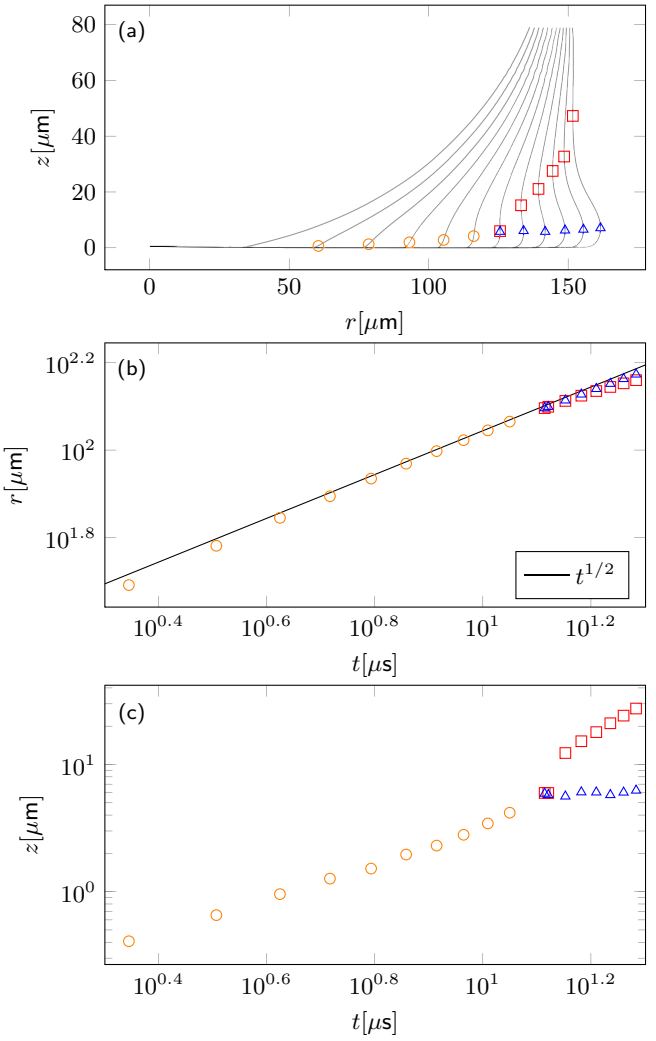

FIG. 13. (a) Interface evolution of droplet impact at 2.5 ms^{-1} with a liquid viscosity ten times that of ethanol. A maximum in the horizontal velocity (○) can be observed on the interface early after impact and can be traced to the time of lamella formation. At the moment of lamella formation there is a bifurcation for points following the cusp (□) and the lamella (△). (b) The radial position plotted as a function of time for the same data points as in (a). The $t^{1/2}$ scaling suggests that the flow is dominated by inertia. (c) The vertical position of the velocity maximum, lamella, and cusp as a function of time.

ethanol droplets. However, this model does not include surface tension and thus does not capture its effect.

One of the predictions of the model is that at early times viscosity is dominant over inertia in the development of the lamella. To further explore the effects of both inertia and viscosity, but also surface tension, in Fig. 13 we examine the early stages of lamella formation. Figure 13(a) shows the interface of a droplet depositing on the surface with a velocity of $v_0 = 2.5$ ms^{-1} and a viscosity of ten times that of ethanol. Between every snapshot of the interface is a time difference of $\Delta t = 2$ μs. Right after impact, a radial velocity maximum (yellow dots) can be observed on the interface; when we track the time evolution of this maximum, eventually a lamella forms at the location of the

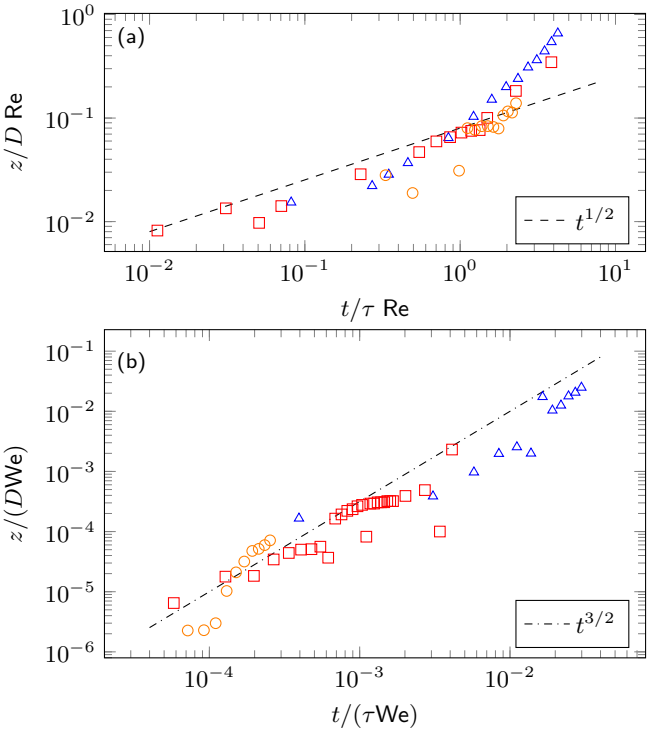

FIG. 14. (a) Nondimensional vertical position of the velocity maximum as a function of nondimensional time for 2.5 ms^{-1} (△), 5.0 ms^{-1} (□), and 10.0 ms^{-1} (○). The surface tension is that of ethanol and the viscosity is ten times that of ethanol. The scaling suggests that at early times, lamella formation is dominated by viscosity. (b) Nondimensional vertical position of the velocity maximum as a function of nondimensional time for 2.5 ms^{-1} (△), 5.0 ms^{-1} (□), and 10.0 ms^{-1} (○). The viscosity is the viscosity of ethanol and the surface tension is 20 times that of ethanol. The scaling suggests that at late times, the scaling for these droplets is dominated by surface tension.

velocity maximum. After the lamella forms, when the radial position of the interface is plotted (r, as a function of the height z), a neck or cusp appears that reflects a minimum of the interface (red dots), and the lamella, which represents a maximum of the interface (blue dots).

Figure 13(b) shows the radial position of these points as a function of time. The scaling with $r \propto t^{1/2}$ is a theoretical prediction based on geometrical arguments and indicates that the radial positions of the velocity maximum and lamella are dominated by inertia. This is consistent with the literature [18]. Figure 13(c) shows the vertical positions of the data points as a function of time.

Figure 14 further explores the evolution of the velocity maximum (i.e., the yellow dots in Fig. 13) for various simulations. In Fig. 14(a) the results are shown for droplets with a viscosity ten times that of ethanol at three different impact velocities. Nondimensionalizing both the vertical position and time with the kinematic viscosity ν and impact velocity v_0 leads to a collapse of the data at early times. This confirms that at early times lamella formation is dominated by viscosity, as is predicted by Mongruel *et al.* [18]. Figure 14(b) shows the results of a droplet with a surface tension of 20 times that of ethanol impacting at three different velocities. This time the axis is scaled using surface tension σ, liquid density ρ, impact velocity v_0, and diameter D. Again, this leads to collapse of the data, suggesting that, for these droplets, late-stage lamella formation is dominated by surface tension. The height of the lamella scales as $z_\sigma \propto \sqrt{\sigma v_0/(\rho D^2)}t^{3/2}$. The fact that the same scaling of the lamella

height before ejection as a function of time can be observed for different material properties in Fig. 12, and for different velocities in Figs. 13 and 14, suggests that a universal mechanism exists that causes the lamella to be created for splashing and depositing droplets. Capturing these different regimes could become a prerequisite for emerging splashing theories, as opposed to a focus on low-viscosity splashes [11,17].

V. CONCLUSIONS

In summary, high-resolution numerical simulations of splashing ethanol droplets appear to describe the so-called "pressure effect" with considerable fidelity. The formation of the experimentally observed central air bubble, air bubble entrainment at the contact line, liquid-sheet formation, and the scaling of the height of the gas film under the droplet with impact velocity are all reproduced.

The results of the simulations are compared with the dewetting theory of Riboux and Gordillo [17], the skating droplet theory of Mandre and Brenner [11], and the lamella formation theory of Mongruel *et al.* [18]. Analyzing the gas film present under the droplet upon impact, no dewetting is observed. Instead, the simulations confirm that there is a thin gas film present under the droplet upon impact. While this gas film is unstable and may collapse, it is always present at the edge of the spreading droplet. This is caused by the contact line moving in a rolling fashion, continuously extending the gas film behind it. The presence of the gas film seems critical for splashing since underresolving the gas film results in the suppression of splashing. In addition, the results of the simulation are consistent with the scaling of the gas film height as a function of impact velocity proposed by Mandre and Brenner [11]. However, the model does not incorporate the effect of liquid viscosity or surface tension. An area for future research is to study the noncontinuum effects in the gas film by investigating the effect of various slip lengths on drainage and collapse of the gas film [20].

While the lamella formation theory does not incorporate surface tension, it does predict the correct scaling of the lamella ejection velocity as a function of the impact velocity for both ethanol and a high-viscosity liquid. Further analysis of the start of the lamella formation right after impact confirms the existence of an early-time viscosity-dominated regime. Also, a different length scale can be defined for the height of the lamella before ejection to incorporate the effect of surface tension in the lamella formation model.

Concerning the breakup of the liquid sheet after ejection, our results are not consistent with the hypothesis that splashing is caused by liquid reflecting on the surface after impact, as proposed in the skating droplet model. However, while the splashing parameter β from the dewetting theory is not found to have a predictive value for our simulations, the results do support the hypothesis that a lifting force acting on the liquid sheet determines whether or not it will break up.

Overall, the different models all provide elements of what is observed in the simulations. The skating droplet model correctly predicts the existence and scaling of a gas film under the droplet and the effect of pressure on the gas film can possibly be captured by using a slip length to model the breakdown of the continuum assumption. The lamella formation theory is able to correctly predict the scaling of the lamella ejection velocity as a function of the impact velocity for various liquids, and lastly, the dewetting theory's hypothesis of a lift force acting on the liquid sheet after ejection is consistent with our results.

ACKNOWLEDGMENTS

This work was supported primarily by the University of Chicago Materials Research Science and Engineering Center, which is funded by the National Science Foundation (NSF) under Award No. DMR-1420709. The authors would like to thank S. R. Nagel, M. Driscoll, C. Stevens, I. Bischofberger, M. Brenner, and S. Rubinstein for many fruitful discussions of the simulation results.

[1] A. L. Yarin, Drop impact dynamics: Splashing, spreading, receding, bouncing..., Annu. Rev. Fluid Mech. **38**, 159 (2006).
[2] L. Xu, W. W. Zhang, and S. R. Nagel, Drop Splashing on a Dry Smooth Surface, Phys. Rev. Lett. **94**, 184505 (2005).
[3] L. Duchemin and C. Josserand, Curvature singularity and film-skating during drop impact, Phys. Fluids **23**, 091701 (2011).
[4] G. Taura and M. Matsumoto, Molecular dynamics simulation of microdroplet impingement on solid surface, J. Fluid Sci. Technol. **5**, 207 (2010).
[5] J. Koplik and R. Zhang, Nanodrop impact on solid surfaces, Phys. Fluids **25**, 022003 (2013).
[6] C. Josserand and S. T. Thoroddsen, Drop impact on a solid surface, Annu. Rev. Fluid Mech. **48**, 365 (2016).
[7] A. K. Price, A. B. MacConnell, and B. M. Paegel, Microfluidic bead suspension hopper, Anal. Chem. **86**, 5039 (2014).
[8] M. M. Driscoll and S. R. Nagel, Ultrafast Interference Imaging of Air in Splashing Dynamics, Phys. Rev. Lett. **107**, 154502 (2011).
[9] A. Latka, Thin-sheet creation and threshold pressures in drop splashing, Soft Matter **13**, 740 (2017).
[10] S. Chandra and C. T. Avedisian, On the collision of a droplet with a solid surface, Proc.: Math. Phys. Sci. 432, 13 (1991).
[11] S. Mandre and M. P. Brenner, The mechanism of a splash on a dry solid surface, J. Fluid Mech. **690**, 148 (2012).
[12] C. D. Stow and M. G. Hadfield, An experimental investigation of fluid flow resulting from the impact of a water drop with an unyielding dry surface, Proc. R. Soc. London, Ser. A **373**, 419 (1981).
[13] C. S. Stevens, Scaling of the splash threshold for low-viscosity fluids, Europhys. Lett. **106**, 24001 (2014).
[14] J. E. Field, J. P. Dear, and J. E. Ogren, The effects of target compliance on liquid drop impact, J. Appl. Phys. **65**, 533 (1989).
[15] M. M. Driscoll, C. S. Stevens, and S. R. Nagel, Thin film formation during splashing of viscous liquids, Phys. Rev. E **82**, 036302 (2010).
[16] A. Marchand, T. S. Chan, J. H. Snoeijer, and B. Andreotti, Air Entrainment by Contact Lines of a Solid Plate Plunged into a Viscous Fluid, Phys. Rev. Lett. **108**, 204501 (2012).
[17] G. Riboux and J. Gordillo, Experiments of Drops Impacting a Smooth Solid Surface: A Model of the Critical Impact Speed for Drop Splashing, Phys. Rev. Lett. **113**, 024507 (2014).
[18] A. Mongruel, V. Daru, F. Feuillebois, and S. Tabakova, Early post-impact time dynamics of viscous drops onto a solid dry surface, Phys. Fluids **21**, 032101 (2009).
[19] J. M. Kolinski, L. Mahadevan, and S. M. Rubinstein, Lift-Off Instability During the Impact of a Drop on a Solid Surface, Phys. Rev. Lett. **112**, 134501 (2014).
[20] J. E. Sprittles, Kinetic Effects in Dynamic Wetting, Phys. Rev. Lett. **118**, 114502 (2017).
[21] C. W. Hirt and B. D. Nichols, Volume of fluid (VOF) method for the dynamics of free boundaries, J. Comput. Phys. **39**, 201 (1981).
[22] H. Rusche, Computational fluid dynamics of dispersed two-phase flows at high phase fractions, Ph.D. thesis, Imperial College, 2002.
[23] J. U. Brackbill, D. B. Kothe, and C. Zemach, A continuum method for modeling surface tension, J. Comput. Phys. **100**, 335 (1992).
[24] T. Qian, X.-P. Wang, and P. Sheng, Molecular scale contact line hydrodynamics of immiscible flows, Phys. Rev. E **68**, 016306 (2003).
[25] J.-F. Gerbeau and T. Lelievre, Generalized Navier boundary condition and geometric conservation law for surface tension, Comput. Methods Appl. Mech. Eng. **198**, 644 (2009).
[26] A. M. P. Boelens and J. J. de Pablo, Generalized navier boundary condition for a volume of fluid approach using a finite-volume method, arXiv:1604.07880.
[27] OpenCFD Ltd., OPENFOAM, version 2.1.1 (2011).
[28] G. K. Batchelor, *An Introduction to Fluid Dynamics*, Cambridge Mathematical Library (Cambridge University Press, Cambridge, UK, 2000).
[29] K. Kadoya, N. Matsunaga, and A. Nagashima, Viscosity and thermal conductivity of dry air in the gaseous phase, J. Phys. Chem. Ref. Data **14**, 947 (1985).

[30] S. G. Jennings, The mean free path in air, J. Aerosol Sci. **19**, 159 (1988).
[31] J. Philippi, P.-Y. Lagrée, and A. Antkowiak, Drop impact on a solid surface: Short-time self-similarity, J. Fluid Mech. **795**, 96 (2016).
[32] I. Bischofberger, K. W. Mauser, and S. R. Nagel, Seeing the invisible—Air vortices around a splashing drop, Phys. Fluids **25**, 091110 (2013).
[33] G. Agbaglah, C. Josserand, and S. Zaleski, Longitudinal instability of a liquid rim, Phys. Fluids **25**, 022103 (2013).
[34] Y. Liu, P. Tan, and L. Xu, Kelvin-Helmholtz instability in an ultrathin air film causes drop splashing on smooth surfaces, Proc. Natl. Acad. Sci. USA **112**, 3280 (2015).
[35] T. M. Squires and S. R. Quake, Microfluidics: Fluid physics at the nanoliter scale, Rev. Mod. Phys. **77**, 977 (2005).
[36] T. C. de Goede, K. G. de Bruin, and D. Bonn, Splashing of impacting drops, arXiv:1701.02504.
[37] C. W. Visser, P. E. Frommhold, S. Wildeman, R. Mettin, D. Lohse, and C. Sun, Dynamics of high-speed micro-drop impact: Numerical simulations and experiments at frame-to-frame times below 100 ns, Soft Matter **11**, 1708 (2015).
[38] J. M. Kolinski, S. M. Rubinstein, S. Mandre, M. P. Brenner, D. A. Weitz, and L. Mahadevan, Skating on a Film of Air: Drops Impacting on a Surface, Phys. Rev. Lett. **108**, 074503 (2012).
[39] A. Latka, A. M. P. Boelens, S. R. Nagel, and J. J. de Pablo, Drop splashing is independent of substrate wetting, Phys. Fluids **30**, 022105 (2018).